Manipulating multiple optical parametric processes in photonic topological insulators

Zhen Jiang,[1,2,*] Bo Ji,[1,2,*] Yanghe Chen,[1,2] Chun Jiang,[1,†] and Guangqiang He[1,2,‡]

[1]*State Key Laboratory of Advanced Optical Communication Systems and Networks, Department of Electronic Engineering, Shanghai Jiao Tong University, Shanghai 200240, China*

[2]*SJTU Pinghu Institute of Intelligent Optoelectronics, Department of Electronic Engineering, Shanghai Jiao Tong University, Shanghai 200240, China*

(Received 21 February 2024; revised 12 April 2024; accepted 26 April 2024; published 13 May 2024)

Topological quantum optics has endowed integrated quantum devices with novel functionalities, including unidirectional transport and immunity to structural defects. Here we propose topological interfaces that support two distinct edge modes with different frequency ranges. The nonlinear four-wave mixing processes in the topological interfaces lead to the generation of signal and idler photons, each corresponding to distinct edge modes. By designing a diamondlike topological structure, we can couple the signal and idler photons into opposite branches, leading to spatial separation of the photon pairs. This behavior enables on-chip generation and flexible control of the topological biphoton states. More importantly, the biphoton states are inborn topologically protected, showing robustness against sharp bends and disorders. Our proposal offers the possibility of robust, multifunctional topological quantum devices, which may find applications in quantum information processing.

DOI: 10.1103/PhysRevB.109.174110

I. INTRODUCTION

The burgeoning field of on-chip quantum light sources has been undergoing revolutionized development thanks to the advancements in nanofabrication technologies. Significant advances in reducing the size and improving the stability through photonic integrated circuits have played a pivotal role in enabling on-chip generation and control of quantum light sources [1]. These improvements have supported more complex and expanding quantum operations, which are crucial for the progress in quantum computing [2,3], quantum communication [4–6], and quantum sensing [7,8]. Two key aspects of on-chip quantum light sources are the amplification of light signals and the generation of entangled photon pairs. Implementing on-chip multifunctional quantum capabilities simultaneously requires precise dispersion engineering and specific materials and is still challenging from a certain perspective.

In parallel, the integration of topological phases into quantum systems is enhanced by the robust guidance and manipulation of light and holds great potential as a cutting-edge and promising area of research [9–11]. This approach is key to the stable generation and transport of quantum states. Topological phases possess a topological nature that provides quantum states with robustness against structural imperfections and disorders. In particular, there have been significant advancements in this field, such as the emergence of topological quantum emitters [12,13], topological quantum interference [14,15], topological biphoton states [16–18], and even topological quantum frequency combs [19,20]. At the same time, emerging advances in topological nonlinear optics also promise topological protection of complex nonlinear processes [21–26]. A significant amount of research has focused on the development of quantum light sources in topological optical systems. However, the study of multifunctional quantum devices in topological photonic systems remains unexplored.

Here we propose integrated topological quantum devices that perform two functions, including optical parametric amplification (OPA) and the entangled biphoton state generation. We demonstrate that a sandwich topological interface emulating the quantum valley Hall (QVH) effect can support two distinct edge modes with different frequency ranges. Using a diamondlike topological structure, we can couple these two edge modes to opposite branches. This allows the spatial separation of signal and idler photons generated from four-wave mixing (FWM) processes. We show that this topological device supports multiple optical parametric processes (OPPs) and can perform two functions: OPA and the generation of continuous frequency entangled biphoton states. Moreover, these biphoton states are robust against defects and sharp bends due to the topological protection of the QVH effect. Our approach expands the potential for on-chip, robust, and multifunctional topological quantum devices and paves the way for new research paths in quantum optics.

II. RESULTS

A. Topological edge modes in kagome lattice

The discovery of the photonic kagome lattice provides a feasible framework for the controllable design of higher-order valley-Hall edge modes [27,28]. Here we explore a two-dimensional topological kagome lattice that supports the generation and flexible control of photonic topological

*These authors contributed equally to this work.
†cjiang@sjtu.edu.cn
‡gqhe@sjtu.edu.cn

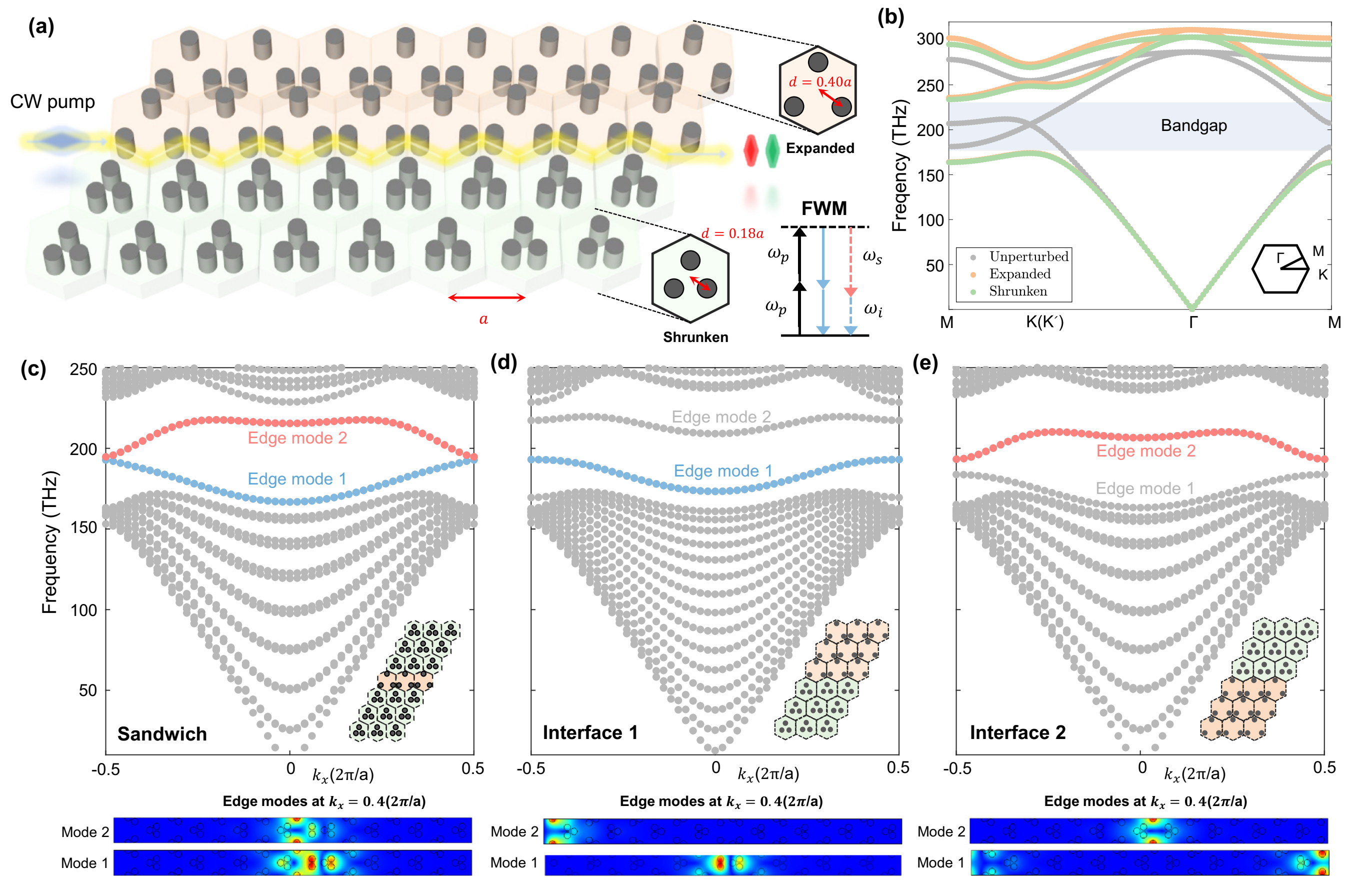

FIG. 1. (a) Scheme of topological design supporting the generation of FWM processes is composed of shrunken ($d = 0.18a$) and expanded ($d = 0.40a$) kagome lattices with C_3 symmetry. (b) Band diagrams of unperturbed (gray dots), shrunken (green dots), and expanded (orange dots) kagome lattices, respectively. Calculated dispersion curves for the (c) sandwich topological interface, (d) topological interface 1, and (e) topological interface 2, respectively. The insets in the lower right corner show schematics of three interfaces composed of shrunken (green region) and expanded (orange region) kagome lattices. The lower insets show the electric field distributions for two edge modes.

quantum states. As depicted in Fig. 1(a), a topological design supporting FWM processes is composed of two kagome lattices (with a lattice constant of $a = 480$ nm) formed by the silicon cylinders ($\epsilon = 12$) in the air background ($\epsilon_0 = 1$). The silicon cylinder has a radius of $0.13a$ and an infinite thickness. The effective topological transition is performed by expanding or shrinking an unperturbed kagome lattice. Figure 1(b) shows the band structures of unperturbed (gray dots), shrunken (green dots), and expanded (orange dots) kagome lattices, respectively. Due to the high symmetry of unperturbed kagome lattices, a Dirac-like degeneracy appears at the two high symmetry points (K and K′ valleys) of the Brillouin zone [28]. The deformation of the unperturbed kagome lattice leads to a complete photonic band gap and band inversion mechanism. Note that the band structures of shrunken ($d = 0.18a$) and expanded ($d = 0.40a$) kagome lattices do not overlap perfectly; this is because the shifts of the dielectric cylinders are not identical.

The kagome lattice exhibits three mirror symmetries: M_x for the x axis and $M_\pm$ for the two lines obtained by rotating the x axis by $\pm 2\pi/3$ [29]. The polarization along the x_i axis represents the expectation value of the position with $p_i = \frac{1}{S}\int_{\mathrm{BZ}} A_i d^2\mathbf{k}$, where $A_i = -i\langle\psi|\partial_{k_i}|\psi\rangle$ denotes the Berry connection with $x_i = x, y$ [29]. The topological bulk polarization describes the shift of the average position of the Wannier center from the center of the unit cell. It is noted that the topological bulk difference of shrunken and expanded kagome lattices corresponds to $P = (0, 0)$ and $P = (1/3, 1/3)$, respectively, which denotes a trivial and nontrivial case, respectively [30].

Due to the bulk-boundary correspondence, the nontrivial polarization difference leads to topological edge states localized at boundaries between the shrunken and expanded kagome lattices. Furthermore, for a finite structure, the deformed kagome lattice is expected to exhibit higher-order topological states such as zero-dimensional corner states [28]. Here we consider a sandwichlike topological interface consisting of a domain of expanded kagome lattices sandwiched between two domains of shrunken kagome lattices. The calculated band structure for this sandwich topological interface is shown in Fig. 1(c). The dispersion curve reveals the presence of two edge modes localized in the topological band gap. Furthermore, it leads to an extensive bandwidth exceeding 40 THz. The lower inset illustrates that these two modes are exclusively confined to the distinct inner boundaries between two types of kagome lattices. This behavior arises from the presence of two boundaries in the sandwich topological interface, which correspond to two topological transitions in the

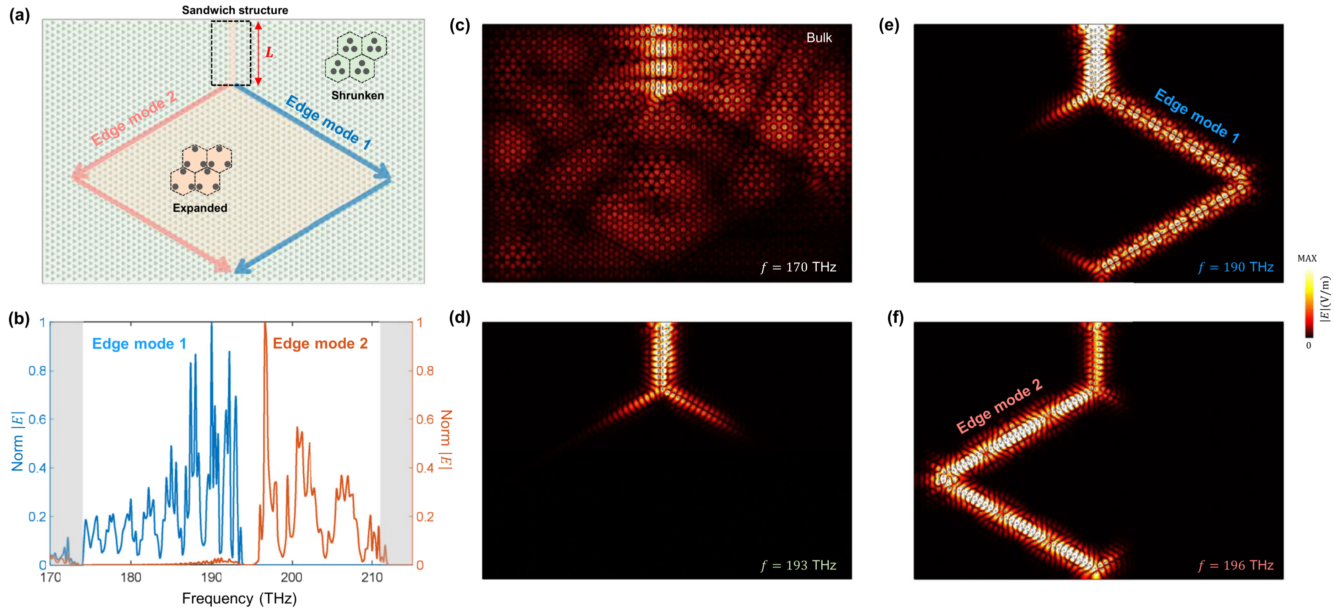

FIG. 2. (a) Scheme of a topological device composed of shrunken (green region) and expanded (orange region) kagome lattices, which contains two parts: a sandwich topological interface (marked by a black dashed box) and a diamondlike topological structure (the length of each side is $30a$). (b) Normalized electric field monitored by two probes placed at the output ports of the two branches in the diamondlike structure. (c)–(f) Field profiles for edge modes at different frequencies in our topological device.

case of trivial-nontrivial-trivial topology. Since the topological band inversion occurs only once at each inner boundary, each boundary supports a single edge mode. As a result, the bands of the two edge modes do not overlap, leading to the formation of a tiny band gap around 193 THz.

We also perform dispersion calculations for the topological interfaces 1 and 2, which contain inverted kagome lattices and exhibit a single boundary. As shown in Figs. 1(d) and 1(e), both of them exhibit two edge modes located within the topological band gap. However, the electric field of two edge modes in each topological interface is localized at the outer and inner boundaries, respectively. Note that the appearance of the outer edge mode is attributed to the application of periodic boundary conditions on the outer boundaries in the simulation model [28]. Correspondingly, the exchange of two kagome lattices leads to the reversion of the topological edge states due to the inversion of the nontrivial polarization difference [29]. The field distribution and dispersion relations indicate that the two distinct edge modes identified in the sandwich topological interface are related to the edge modes (localized at the inner boundary) of topological interfaces 1 and 2, respectively. The mode-matching behavior simplifies the process of coupling edge modes from the sandwich topological interface to other topological interfaces. Due to the distinct frequency ranges of the two edge modes, the coupling between different modes achieves a frequency-dependent filtering capability. In other words, the frequency division characteristic enables the realization of multifunctional on-chip topological photonic devices, which may find applications in areas such as optical transmission and light source generation.

Accordingly, we design a topological device composed of shrunken (green region) and expanded (orange region) kagome lattices, which contains two parts: a sandwich topological interface (marked by a black dashed box) with a length of L and a diamondlike topological structure [Fig. 2(a)]. It is important to highlight that, in this design, the branches of the diamondlike structure exhibit distinct topological edge modes as a result of the mirror symmetry of the lattices. For the sandwich topological interface region, there are two allowed edge modes with different frequency ranges. However, for the diamondlike structure, the two branches correspond to topological interfaces 1 and 2, respectively. Therefore, the light can be efficiently transmitted to the left and right branches with the frequency range of $f > 193$ THz and $f < 193$ THz, respectively.

To get deeper insights into the characteristics of topological edge modes, we simulate the field profiles in this diamondlike structure at different frequencies. As shown in Figs. 2(c)–2(f), the energy couples to the opposite branch corresponding to different pump frequencies. We set two probes positioned at the output ports of two branches to monitor the field intensity. Figure 2(b) shows the simulated transmission spectra of the light, which clearly shows the frequency splitting functionality of our design. The presence of a frequency gap, characterized by the absence of power detected at either output port, results from the competition between the two edge modes. Accordingly, as shown in Fig. 2(d), the light does not engage with any branch at the specific frequency of around 193 THz. The result is consistent with the dispersion relation shown in Fig. 1(c). It is worth mentioning that this dichroic mirror behavior has the potential to facilitate a range of innovative topological functionalities.

B. Multiple OPPs in topological devices

Due to the fascinating functionalities of the diamondlike topological structure, we expect stable generation and

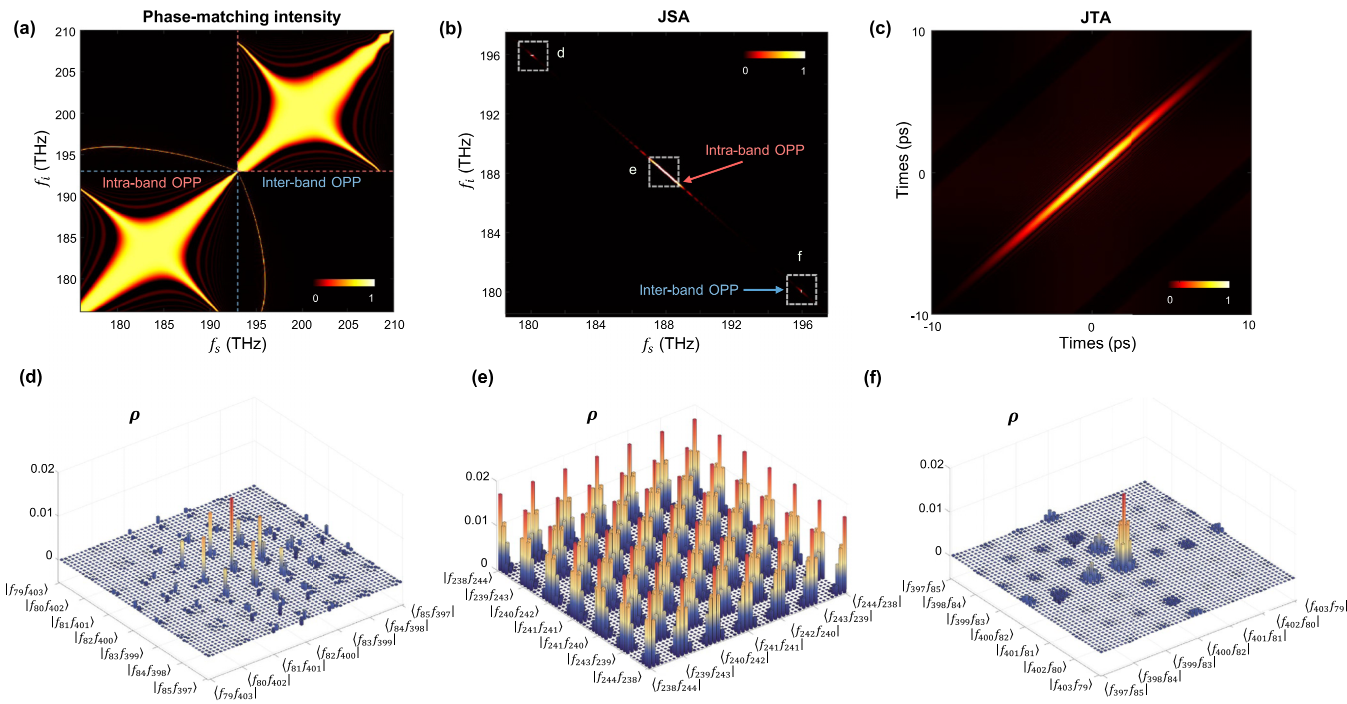

FIG. 3. (a) Phase-matching intensity distribution of FWM processes in the sandwich topological interface. (b) JSA distribution and (c) corresponding JTA distribution characterizing the biphoton state generated in the sandwich topological interface, where the color bar indicates the magnitude. (d)–(f) Three parts of the density matrix ρ of the quantum state corresponding to three regions (labeled by d, e, and f, respectively) in (b), where the coordinates in the horizontal plane denote different projection bases.

flexible manipulation of topological quantum states. Due to the absence of second-order nonlinearity of silicon, we only consider the FWM processes (third-order nonlinear effect). The nonlinear FWM processes generated in the sandwich topological interface can lead to the signal and idler photons. To ensure the topological transport of biphoton states, the frequencies of the pump, signal, and idler modes should be within the operation bandwidth of the topological edge modes. The energy and momentum conversion equations that govern the FWM processes are defined as $2\omega_p = \omega_s + \omega_i$ and $2k_p = k_s + k_i$, where $\omega_{p,s,i}$ and $k_{p,s,i}$ represent the frequencies and wave vectors of the pump, signal, and idler, respectively. In general, the Hamiltonian for the FWM process in the topological waveguide can be written as

$$\hat{H}_{\mathrm{NL}} = \hat{H}_{\mathrm{SPM}} + \hat{H}_{\mathrm{XPM}} + \hat{H}_{\mathrm{FWM}}, \tag{1}$$

where $\hat{H}_{\mathrm{SPM}}$, $\hat{H}_{\mathrm{XPM}}$, and $\hat{H}_{\mathrm{FWM}}$ denote the self-phase modulation (SPM), cross-phase modulation (XPM), and FWM processes, respectively. The SPM and XPM terms affect the oscillation process. Due to the frequency division of our diamondlike topological structure, the left and right branches correspond to the OPA process and entangled biphoton generation, respectively [30].

By matching the frequencies of FWM processes with the operating bandwidths of topological edge states, it becomes possible to implement topological protection of entangled biphoton states [16–18], and even quantum frequency combs [19,20]. The dispersion engineering of topological edge states offers a possible method for manipulating FWM processes within the topological band gap [16]. To satisfy the momentum conversion condition for FWM processes, the wave vector mismatch $\Delta k = 2k_p - k_s - k_i$ must be taken into account. Note that the energy conversion of FWM processes is significantly improved when the wave vector mismatch satisfies $\Delta k = 0$. The phase-matching intensity of FWM processes is given by $\mathrm{PM} = \mathrm{sinc}(\frac{\Delta k L}{2})$, where L is the length of the topological interface [41].

The phase-matching intensity distribution of FWM processes in the sandwich topological interface is depicted in Fig. 3(a), demonstrating three cases of phase matching. The two main bright regions correspond to the intraband OPPs of the two edge modes themselves. However, besides the intraband OPP, an additional phase-matching case (bright curves) is also observed, corresponding to the interband OPP between two edge modes. The nonlinear interactions between two edge modes result in mode conversion, which can lead to significant correlations between different transverse modes.

By pumping the sandwich topological waveguide with the frequency of 188 THz, we can calculate the joint spectral amplitude (JSA) of the biphoton state generated from the FWM process. Such a biphoton state can be given by

$$|\Psi\rangle = \iint d\omega_s d\omega_i \mathcal{A}(\omega_s, \omega_i) \hat{a}_s^\dagger(\omega_s) \hat{a}_i^\dagger(\omega_i) |0\rangle, \tag{2}$$

where $\hat{a}_s^\dagger$ and $\hat{a}_i^\dagger$ are creation operators for photons and $\mathcal{A}(\omega_s, \omega_i)$ is the JSA. The JSA is governed by $\mathcal{A}(\omega_s, \omega_i) = \alpha(\frac{\omega_s+\omega_i}{2})\,\mathrm{sinc}(\frac{\Delta k L}{2})$, where the pump spectrum is $\alpha(\frac{\omega_s+\omega_i}{2})$ and joint phase-matching spectrum is $\mathrm{sinc}(\frac{\Delta k L}{2})$. The pump is Gaussian with a frequency center of $f_p = 188$ THz and full width at half maximum of $\Delta f_p = 115$ GHz.

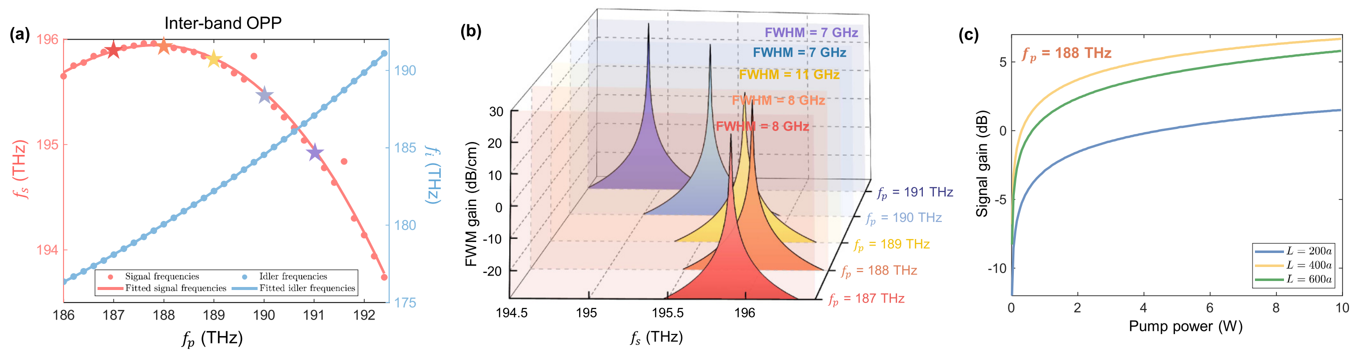

FIG. 4. (a) Frequencies of the signal and idler modes resulting from the interband OPP at different pump frequencies. (b) FWM gain coefficient corresponding to interband OPP at different pump frequencies for a $400a$ length topological waveguide (1 W pump power). (c) Signal gain as a function of pump power for the waveguide length with $L = 200a$, $400a$, and $600a$, respectively.

Consequently, the JSA characterizing the biphoton state generated in the sandwich topological interface is plotted in Fig. 3(b), where the main intensity region (corresponding to intraband OPP) along the diagonal axis denotes a strong signal-idler correlation in the frequency domain [16]. Notably, two additional bright spots are symmetrically located above and below the central line, indicating the presence of interband OPP. The spotlike phase-matching intensity distribution is also proven to be a perfect case for a heralded single photon generator [41] and, also, its purity can be improved by machine learning methods [42,43]. These points indicate the existence of frequency correlations resulting from the additional interband OPP interaction between edge mode 1 and edge mode 2. Note that the signal mode frequency is larger than 193 THz, so the generated signal can pass through the left branch while the generated idler passes through the right branch. The potential phase-matching conditions between two different topological edge states promise many effective solutions for manipulating photonic topological quantum states.

As a conjugate variable of the frequency, we can obtain the joint temporal amplitude (JTA) of the biphotons from the Fourier transform of the JSA by $\tilde{\mathcal{A}}(t_s, t_i) = \mathcal{F}[\mathcal{A}(\omega_i, \omega_s)]$ [43]. The peak intensity of the JTA is located at $\Delta\tau_y = \Delta\tau_z = 0$, indicating a relative phase value of $\phi = 0$ [Fig. 3(c)]. The biphoton state exhibits a signal-idler time correlation with a bandwidth of 10 ps.

Furthermore, we analyze the photonic topological quantum states by implementing quantum state tomography on a set of bases. We discretize the frequencies of the signal and idler modes in the JSA into 681 frequency modes, denoted as f_i, where $i = 1, 2, 3, \ldots, 681$. Based on the JSA, we can calculate the density matrix of the quantum state by $\rho = |\Psi\rangle\langle\Psi|$, with projection bases of $|f_1 f_1\rangle, |f_1 f_2\rangle, |f_1 f_3\rangle, \ldots, |f_{681} f_{681}\rangle$. Given its considerable size, we plot three parts of the density matrix (comprising 49 projection bases) in Figs. 3(d)–3(f) [corresponding to three dashed boxes in Fig. 3(b)]. The two density matrices [Figs. 3(d) and 3(f)] clearly demonstrate the emergence of the interband OPP.

C. Interband OPP: Tunable OPA

Our topological scheme supporting multiple OPPs provides a different approach to the manipulation of quantum functional devices. Here we implement an OPA by the FWM with interband OPP, where the frequency division of the diamondlike structure leads to spatial separation of signal photons. This spatial separation behavior allows for the direct extraction of amplified optical signals since the generated signal could pass through the left branch of the diamondlike structure ($f_s > 193$ THz). We investigate the frequencies of the signal and idler modes resulting from the interband OPP with different pump frequencies. As shown in Fig. 4(a), the tunable range of the signal mode extends from 193.5 THz to 196 THz, achieving a tunable range of 2.5 THz.

Typically, signal and strong pump modes are coupled into the topological waveguide, where the signal power is amplified via degenerate FWM processes [44]. The FWM gain coefficient is given by $g = \sqrt{\gamma P_p \Delta k - (\Delta k/2)^2}$, where $\gamma = \omega_p n_2 / c A_{\text{eff}}$ is the effective nonlinearity of the topological waveguide, P_p is the pump power, n_2 is Kerr nonlinearity, A_{eff} is the nonlinear effective area, and c is the speed of light. The effective amplification in the waveguide requires strict adherence to a specific phase-matching condition due to the coherent nature of the parametric interaction. Figure 4(b) illustrates the FWM gain coefficient corresponding to interband OPP at different pump frequencies for a $400a$ length topological waveguide (1 W pump power). The interband OPP allows for a supernarrow bandwidth of high gain with a full width at half maximum (FWHM) of around 8 GHz. At the center frequency of the gain region, the FWM gain coefficient of up to 30 dB/cm can be achieved and the intensity of the FWM gain peak is constant during the tuning of the pump frequency. Such a narrow-bandwidth tunable OPA can be used to amplify signals from a single-photon source.

Consider a pump wave experiencing SPM, while cross-phase modulation XPM occurs in both signal and idle modes. Therefore, the nonlinear phase mismatch caused by SPM and XPM should be taken into account and the updated phase mismatch is given by $\Delta k_{all} = 2\gamma P_p - \Delta k$ [45]. Neglecting optical propagation loss, the observed signal gain generated via FWM for interband OPP can be written as [34]

$$G_s = \frac{P_s(L)}{P_s(0)} = 1 + \left(\frac{\gamma P_p}{g}\sinh(gL)\right)^2, \tag{3}$$

where $P_s(L)$ and $P_s(0)$ are the output and input signal powers, respectively. In Fig. 4(c), we plot the signal gain as a function of pump power for the waveguide length with

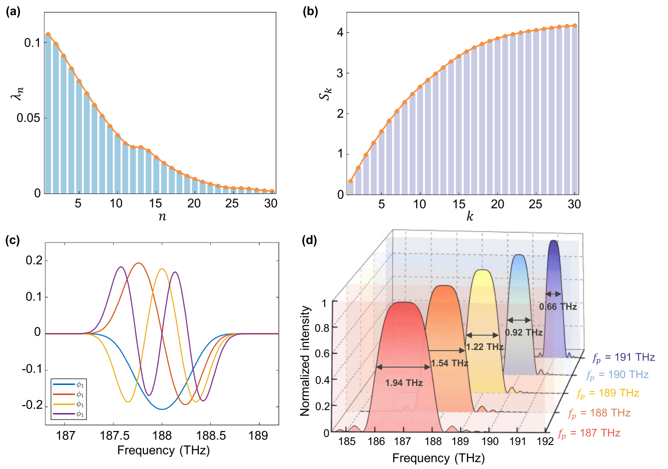

FIG. 5. Distribution of (a) normalized Schmidt coefficients λ_n and (b) entanglement entropy S_k for the biphoton state generated from intraband OPP. (c) Eigenfunctions ϕ_n ($n = 1, 2, 3, 4$) for the biphoton state. (d) Normalized two-photon spectral distribution with varying pump frequencies.

$L = 200a$, $400a$, and $600a$, respectively. For a topological waveguide with $L = 400a$, a peak signal gain of 5 dB can be achieved when the pump power exceeds 4 W. Note that when the gain of an OPA is large, the generated signal photons can be significantly amplified, reaching macroscopic levels through a phenomenon known as optical parametric generation. The expected number of photons at the output is given by $\langle n\rangle = \sinh^2(gL) \approx 0.25\,\exp(2gL)$ [46]. The detailed quantum analysis of the OPA in our topological device is shown in Supplemental Sec. II [30]. Such a quantum OPA can be used in squeezing light detection [47] and optical homodyne measurement [48].

D. Intraband OPP: Entangled biphoton state generation

Furthermore, we can expect the generation and manipulation of a frequency entangled biphoton state derived from the intraband OPP. Note that all pump, signal, and idler modes can couple into the right branch of the diamondlike topological structure ($f_s, f_i < 193$ THz), which is convenient for extracting broadband entangled photon pairs directly at this branch. We use the Schmidt decomposition to evaluate the separability of the JSA without considering part of the phase information [37,49]. Figures 5(a) and 5(b) show the distributions of normalized Schmidt coefficients λ_n and entanglement entropy S_k, respectively. Note that the Schmidt coefficients λ_n indicate the probability of acquiring the nth quantum state. Nonzero coefficients (greater than 1) indicate the frequency entanglement [37,50]. Moreover, the entanglement entropy, denoted by $S_k = -\sum \lambda_n \log_2 \lambda_n$, and the Schmidt number, represented by $K = (\sum \lambda_n^2)^{-1}$, are reliable methods for measuring the degree of entanglement [49]. The entanglement of a topological quantum state can be verified by $S_k > 0$ or $K > 1$, where a higher value of S_k and K indicates a high-quality of frequency entanglement. For our topological quantum state, the calculated values for Schmidt number and entanglement entropy are $K = 16.24$ and $S_k = 4.42$, respectively, which indicates the emergence of a high-quality frequency entangled biphoton state in the sandwich topological interface.

Due to the symmetry between the signal and idler photons, the eigenfunctions ϕ and ψ in the Schmidt decomposition have the same form. The initial four eigenfunctions ϕ_n ($n = 1, 2, 3, 4$) are shown in Fig. 5(c), which indicates the orthogonality of each basis function. Also, the number of photon pairs generated by the FWM process is given by

$$\begin{aligned} S(\omega) &= \langle\Psi|a_s^\dagger a_i^\dagger a_i a_s|\Psi\rangle \\ &= \frac{\eta^2}{c^2}\int \mathrm{d}\omega_\mathrm{s} \int \mathrm{d}\omega_\mathrm{i} |\mathcal{A}(\omega_\mathrm{s}, \omega_\mathrm{i})|^2, \end{aligned} \tag{4}$$

where a_s and a_i are annihilation operators for photons and η is a constant term. Correspondingly, we calculate the normalized two-photon spectral distribution with pump at different frequencies. As shown in Fig. 5(d), the 3 dB bandwidths of the two-photon spectrum are 1.94, 1.54, 1.22, 0.92, and 0.66 THz, respectively, demonstrating the tunability of the spectral bandwidth. This high-dimensional topological quantum entangled state with tunable spectral bandwidth enables complex and large-scale quantum simulations and computations.

Alternatively, the single-photon purity associated with the factorization of biphoton states can be implemented by Schmidt decomposition. Purity plays a crucial role in achieving highly visible quantum interference between photons generated from the same source. In general, single-photon purity is expressed as $\mathrm{Tr}(\hat{\rho}_\mathrm{s}^2)$, where $\hat{\rho}_\mathrm{s} = \mathrm{Tr}_\mathrm{i}(|\Psi\rangle\langle\Psi|)$ represents the density operator for the heralded single photon and Tri is the trace over the idler mode. The heralded single-photon purity, denoted as $\mathrm{Tr}(\hat{\rho}_\mathrm{s}^2)$, can be calculated by $\mathrm{Tr}(\hat{\rho}_\mathrm{s}^2) = K^{-1}$ [51]. Consequently, the single-photon purity for our topological quantum state is calculated to be 0.06, corresponding to a highly inseparable quantum state.

E. Robustness against disorders for FWM processes

To verify the topological protection of nonlinear FWM processes, we simulate the FWM process in the diamondlike topological structure with CW pump excitation [11,21] employing COMSOL MULTIPHYSICS software (see Methods). In our numerical model, we use a point source localized at the input port to excite topological edge modes. Notably, there is no input for the idler mode; the excitation of idler modes reveals the generation of stimulated FWM processes [11]. Here the frequencies of the pump, signal, and idler modes are chosen as $f_s = 196$ THz, $f_p = 188$ THz, and $f_i = 180$ THz, respectively. As depicted in Figs. 6(a)–6(c), the field profiles of topological edge modes at the idler frequency provide clear evidence of the simulated FWM process. Most importantly, due to their different frequencies, the pump and signal modes couple into the right branch of the diamondlike structure, while the generated idler mode couples into the left branch. As a result, the photon pairs are separated, with an idler photon being extracted during the FWM process.

In addition, we incorporate a diamondlike topological structure to extend the capacity of our system to a larger spatial domain, allowing for improved manipulation of the

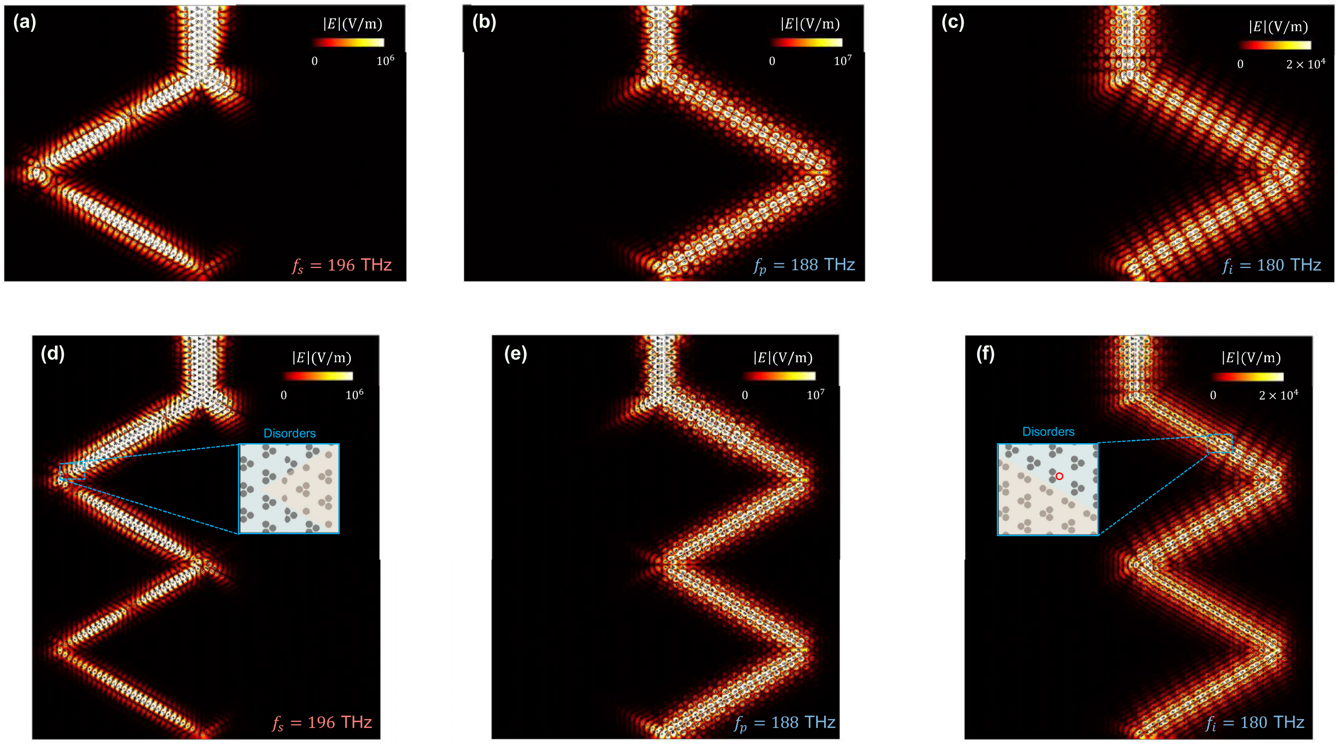

FIG. 6. Field profiles of the FWM process in the diamondlike topological structure at the frequencies of the (a) signal mode ($f_s = 196$ THz), (b) pump mode ($f_p = 188$ THz), and (c) idler mode($f_i = 180$ THz), respectively. Field profiles of the stimulated FWM process in the expanded diamondlike topological structure at the frequencies of the (d) signal mode ($f_s = 196$ THz), (e) pump mode ($f_p = 188$ THz), and (f) idler mode ($f_i = 180$ THz), respectively. The red empty circle marked in (f) denotes the removed cylinder.

transmission routes of photonic topological quantum states. As shown in Figs. 6(d)–6(f), within the blue region, the position of a rod is randomly shifted by distances between $-0.1a$ and $0.2a$ (left branch) and a rod is randomly removed (right branch). The idler mode generated by FWM processes also shows strong localization along arbitrary topological boundaries. The results reveal that the topological nature of the QVH effect brings robustness to the FWM process against sharp bends and defects. These intriguing behaviors enable the manipulation of the two-photon state's path and the flexible extraction of individual photons.

III. CONCLUSION

In this work, we demonstrate on-chip topological quantum optical devices capable of performing multiple functions including OPA and entangled biphoton generation. We show that there exist two distinct edge modes corresponding to different frequency ranges in the sandwich topological interface. By employing a diamond structure, we can couple these two edge modes into separate branches to achieve the separation of spatial modes. Due to the coexistence of two edge modes, the FWM process enables two types of OPPs, corresponding to interband and intraband cases, respectively. More importantly, thanks to distinct transmission paths of the edge modes, these two OPPs can individually facilitate quantum OPA and the generation of continuous frequency-entangled photon pairs along separate branches. In addition, these quantum processes exhibit topological protection properties, showing robustness to defects and sharp bends. Our proposal offers enhanced possibilities for on-chip robust, multifunctional topological quantum devices.

IV. METHODS

A. Numerical simulation

We use the finite-element method solver COMSOL MULTIPHYSICS to perform numerical simulations. The band diagrams [Fig. 1(b)] and dispersion curves [Figs. 1(c)–1(e)] of topological photonic crystals are calculated by solving the eigenfrequencies with periodic boundary conditions. Here we consider the field profiles of transverse magnetic (TM) polarization modes. In the simulation of the electric field profile [Figs. 2(c)–2(f)], we construct the diamondlike topological structure in the frequency domain solver and then use a point source to excite the edge states. The simulated nonlinear FWM processes (Fig. 6) are performed by using the third-order nonlinearity of silicon $\chi^{(3)} = 5 \times 10^{-18}$ m^2/V^2. The FWM process in the sandwich topological interface can be described by

$$\begin{aligned}
\mathbf{P}_p(\omega_s + \omega_i - \omega_p) &= 6\varepsilon_0\chi^{(3)}E_sE_iE_p^*,\\
\mathbf{P}_s(\omega_p + \omega_p - \omega_i) &= 3\varepsilon_0\chi^{(3)}E_pE_pE_i^*,\\
\mathbf{P}_i(\omega_p + \omega_p - \omega_s) &= 3\varepsilon_0\chi^{(3)}E_pE_pE_s^*,
\end{aligned} \tag{5}$$

where ε_0 is the vacuum permittivity and $\mathbf{P}_{p,s,i}$ and $E_{p,s,i}$ are the polarization and electric field of the pump, signal, and idler, respectively. The frequencies of the pump, signal, and idler modes are chosen as $f_s = 196$ THz, $f_p = 188$ THz, and $f_i = 180$ THz, respectively. A point source localized at the input port is used to excite the pump and signal modes, while there is no input for the idler mode. Due to the coupling of three electromagnetic models at the pump and signal frequencies, the excitation of idler modes reveals the generation of stimulated FWM processes [11,21].

B. Theoretical analysis of interband OPP

In our diamondlike topological device, the interband OPP in the sandwich topological interface leads to an OPA process. Note that only the signal mode can be coupled into the left branch, which is more beneficial for the extraction of the amplified signal. From the nonlinear Hamiltonian [Eq. (2)], we can derive the Heisenberg equations for the pump, signal, and idler modes [11]. By substituting the operators in the Heisenberg equations with classical light fields, the coupled equations for these three modes can be given by

$$\begin{aligned}\frac{dA_p}{dx} =& i\gamma\{[|A_p|^2 + 2(|A_s|^2 + |A_i|^2)]A_p\\ &+ 2A_sA_iA_p^*\exp(i\Delta kx)\},\\ \frac{dA_s}{dx} =& i\gamma\{[|A_s|^2 + 2(|A_i|^2 + |A_p|^2)]A_s\\ &+ A_i^*A_p^2\exp(-i\Delta kx)\},\\ \frac{dA_i}{dx} =& i\gamma\{[|A_i|^2 + 2(|A_s|^2 + |A_p|^2)]A_i\\ &+ A_s^*A_p^2\exp(-i\Delta kx)\}, \end{aligned} \tag{6}$$

where $A_j(x)$, $j \in \{p, s, i\}$ is the amplitude of the light field. Solving the coupled equations enables the amplification of a weak signal as it propagates along the topological waveguide; we can get an analytical solution

$$P_s(L) = P_s(0)\left(1 + \left[\frac{\gamma P_p}{g}\sinh(gL)\right]^2\right). \tag{7}$$

With this equation, we can calculate the power of the signal light after it has propagated a distance L through the topological waveguide. Therefore, the signal gain can be given by [34]

$$G_s = \frac{P_s(L)}{P_s(0)} = 1 + \left(\frac{\gamma P_p}{g}\sinh(gL)\right)^2. \tag{8}$$

ACKNOWLEDGMENTS

This work is supported by the National Key Research and Development Program of China (2021YFB2800401), Key-Area Research and Development Program of Guangdong Province (Grant No. 2018B030325002), the National Natural Science Foundation of China (Grant No. 62075129), the SJTU Pinghu Institute of Intelligent Optoelectronics (Grant No. 2022SPIOE204), and the Sichuan Provincial Key Laboratory of Microwave Photonics (2023-04).

The authors declare no competing interests.

[1] G. Moody, L. Chang, T. J. Steiner, and J. E. Bowers, Chip-scale nonlinear photonics for quantum light generation, AVS Quantum Sci. **2**, 041702 (2020).

[2] J. L. O'brien, Optical quantum computing, Science **318**, 1567 (2007).

[3] L. Caspani, C. Xiong, B. J. Eggleton, D. Bajoni, M. Liscidini, M. Galli, R. Morandotti, and D. J. Moss, Integrated sources of photon quantum states based on nonlinear optics, Light Sci. Appl. **6**, e17100 (2017).

[4] P. Sibson, C. Erven, M. Godfrey, S. Miki, T. Yamashita, M. Fujiwara, M. Sasaki, H. Terai, M. G. Tanner, C. M. Natarajan *et al.*, Chip-based quantum key distribution, Nat. Commun. **8**, 13984 (2017).

[5] X. Lu, Q. Li, D. A. Westly, G. Moille, A. Singh, V. Anant, and K. Srinivasan, Chip-integrated visible–telecom entangled photon pair source for quantum communication, Nat. Phys. **15**, 373 (2019).

[6] A. Orieux and E. Diamanti, Recent advances on integrated quantum communications, J. Opt. **18**, 083002 (2016).

[7] S. Pirandola, B. R. Bardhan, T. Gehring, C. Weedbrook, and S. Lloyd, Advances in photonic quantum sensing, Nat. Photon. **12**, 724 (2018).

[8] C. L. Degen, F. Reinhard, and P. Cappellaro, Quantum sensing, Rev. Mod. Phys. **89**, 035002 (2017).

[9] Y. Wang, K. D. Jöns, and Z. Sun, Integrated photon-pair sources with nonlinear optics, Appl. Phys. Rev. **8**, 011314 (2021).

[10] Q. Yan, X. Hu, Y. Fu, C. Lu, C. Fan, Q. Liu, X. Feng, Q. Sun, and Q. Gong, Quantum topological photonics, Adv. Opt. Mater. **9**, 2001739 (2021).

[11] J. W. You, Z. Lan, Q. Ma, Z. Gao, Y. Yang, F. Gao, M. Xiao, and T. J. Cui, Topological metasurface: From passive toward active and beyond, Photon. Res. **11**, B65 (2023).

[12] S. Barik, A. Karasahin, C. Flower, T. Cai, H. Miyake, W. DeGottardi, M. Hafezi, and E. Waks, A topological quantum optics interface, Science **359**, 666 (2018).

[13] S. Mittal, E. A. Goldschmidt, and M. Hafezi, A topological source of quantum light, Nature (London) **561**, 502 (2018).

[14] S. Mittal, V. V. Orre, E. A. Goldschmidt, and M. Hafezi, Tunable quantum interference using a topological source of indistinguishable photon pairs, Nat. Photon. **15**, 542 (2021).

[15] Y. Chen, X.-T. He, Y.-J. Cheng, H.-Y. Qiu, L.-T. Feng, M. Zhang, D.-X. Dai, G.-C. Guo, J.-W. Dong, and X.-F. Ren, Topologically protected valley-dependent quantum photonic circuits, Phys. Rev. Lett. **126**, 230503 (2021).

[16] Z. Jiang, Y. Ding, C. Xi, G. He, and C. Jiang, Topological protection of continuous frequency entangled biphoton states, Nanophotonics **10**, 4019 (2021).

[17] T. Dai, Y. Ao, J. Bao, J. Mao, Y. Chi, Z. Fu, Y. You, X. Chen, C. Zhai, B. Tang *et al.*, Topologically protected quantum entanglement emitters, Nat. Photon. **16**, 248 (2022).

[18] S. Afzal, T. J. Zimmerling, M. Rizvandi, M. Taghavi, T. Hrushevskyi, M. Kaur, V. Van, and S. Barzanjeh, Bright

quantum photon sources from a topological floquet resonance, arXiv:2308.11451.

[19] Z. Jiang, Y. Chen, C. Jiang, and G. He, Generation of quantum optical frequency combs in topological resonators, Adv. Quantum Technol. **7**, 2300354 (2024).

[20] Z. Jiang, H. Wang, Y. Yang, Y. Shen, B. Ji, Y. Chen, Y. Zhang, L. Sun, Z. Wang, C. Jiang *et al.*, On-chip topological transport of optical frequency combs in silicon-based valley photonic crystals, arXiv:2310.15629.

[21] J. W. You, Z. Lan, and N. C. Panoiu, Four-wave mixing of topological edge plasmons in graphene metasurfaces, Sci. Adv. **6**, eaaz3910 (2020).

[22] D. Smirnova, S. Kruk, D. Leykam, E. Melik-Gaykazyan, D.-Y. Choi, and Y. Kivshar, Third-harmonic generation in photonic topological metasurfaces, Phys. Rev. Lett. **123**, 103901 (2019).

[23] T. Dai, Y. Ao, J. Mao, Y. Yang, Y. Zheng, C. Zhai, Y. Li, J. Yuan, B. Tang, Z. Li *et al.*, Non-hermitian topological phase transitions controlled by nonlinearity, Nat. Phys. **20**, 101 (2023).

[24] D. Smirnova, D. Leykam, Y. Chong, and Y. Kivshar, Nonlinear topological photonics, Appl. Phys. Rev. **7**, 021306 (2020).

[25] Z. Jiang, L. Zhou, W. Li, Y. Li, L. Feng, T. Wu, C. Jiang, and G. He, Topological dissipative Kerr soliton combs in a valley photonic crystal resonator, Phys. Rev. B **108**, 205421 (2023).

[26] S. Mittal, G. Moille, K. Srinivasan, Y. K. Chembo, and M. Hafezi, Topological frequency combs and nested temporal solitons, Nat. Phys. **17**, 1169 (2021).

[27] A. Vakulenko, S. Kiriushechkina, M. Wang, M. Li, D. Zhirihin, X. Ni, S. Guddala, D. Korobkin, A. Alù, and A. B. Khanikaev, Near-field characterization of higher-order topological photonic states at optical frequencies, Adv. Mater. **33**, 2004376 (2021).

[28] M. Li, D. Zhirihin, M. Gorlach, X. Ni, D. Filonov, A. Slobozhanyuk, A. Alù, and A. B. Khanikaev, Higher-order topological states in photonic kagome crystals with long-range interactions, Nat. Photon. **14**, 89 (2020).

[29] M. Ezawa, Higher-order topological insulators and semimetals on the breathing kagome and pyrochlore lattices, Phys. Rev. Lett. **120**, 026801 (2018).

[30] See Supplemental Material at http://link.aps.org/supplemental/10.1103/PhysRevB.109.174110 for (i) topological kagome lattice, (ii) theoretical analysis of two opps in topological devices, and (iii) implementing multiple opps in honeycomb lattices, which includes Refs. [31–40].

[31] X. Ni, M. Weiner, A. Alu, and A. B. Khanikaev, Observation of higher-order topological acoustic states protected by generalized chiral symmetry, Nat. Mater. **18**, 113 (2019).

[32] R. D. King-Smith and D. Vanderbilt, Theory of polarization of crystalline solids, Phys. Rev. B **47**, 1651 (1993).

[33] A. L. Gaeta, M. Lipson, and T. J. Kippenberg, Photonic-chip-based frequency combs, Nat. Photon. **13**, 158 (2019).

[34] J. Hansryd, P. A. Andrekson, M. Westlund, J. Li, and P.-O. Hedekvist, Fiber-based optical parametric amplifiers and their applications, IEEE J. Sel. Top. Quantum Electron. **8**, 506 (2002).

[35] G. Cappellini and S. Trillo, Third-order three-wave mixing in single-mode fibers: exact solutions and spatial instability effects, J. Opt. Soc. Am. B **8**, 824 (1991).

[36] R. Stolen and J. Bjorkholm, Parametric amplification and frequency conversion in optical fibers, IEEE J. Quantum Electron. **18**, 1062 (1982).

[37] C. K. Law, I. A. Walmsley, and J. H. Eberly, Continuous frequency entanglement: effective finite hilbert space and entropy control, Phys. Rev. Lett. **84**, 5304 (2000).

[38] Y. Yang, Y. Yamagami, X. Yu, P. Pitchappa, J. Webber, B. Zhang, M. Fujita, T. Nagatsuma, and R. Singh, Terahertz topological photonics for on-chip communication, Nat. Photon. **14**, 446 (2020).

[39] J. Lu, C. Qiu, L. Ye, X. Fan, M. Ke, F. Zhang, and Z. Liu, Observation of topological valley transport of sound in sonic crystals, Nat. Phys. **13**, 369 (2017).

[40] J. Noh, S. Huang, K. P. Chen, and M. C. Rechtsman, Observation of photonic topological valley Hall edge states, Phys. Rev. Lett. **120**, 063902 (2018).

[41] P. J. Mosley, J. S. Lundeen, B. J. Smith, P. Wasylczyk, A. B. U'Ren, C. Silberhorn, and I. A. Walmsley, Heralded generation of ultrafast single photons in pure quantum states, Phys. Rev. Lett. **100**, 133601 (2008).

[42] C. Cui, R. Arian, S. Guha, N. Peyghambarian, Q. Zhuang, and Z. Zhang, Wave-function engineering for spectrally uncorrelated biphotons in the telecommunication band based on a machine-learning framework, Phys. Rev. Appl. **12**, 034059 (2019).

[43] W.-H. Cai, Y. Tian, S. Wang, C. You, Q. Zhou, and R.-B. Jin, Optimized design of the lithium niobate for spectrally-pure-state generation at mir wavelengths using metaheuristic algorithm, Adv. Quantum Technol. **5**, 2200028 (2022).

[44] J. Riemensberger, N. Kuznetsov, J. Liu, J. He, R. N. Wang, and T. J. Kippenberg, A photonic integrated continuous-travelling-wave parametric amplifier, Nature (London) **612**, 56 (2022).

[45] M. A. Foster, A. C. Turner, J. E. Sharping, B. S. Schmidt, M. Lipson, and A. L. Gaeta, Broad-band optical parametric gain on a silicon photonic chip, Nature (London) **441**, 960 (2006).

[46] L. Ledezma, R. Sekine, Q. Guo, R. Nehra, S. Jahani, and A. Marandi, Intense optical parametric amplification in dispersion-engineered nanophotonic lithium niobate waveguides, Optica **9**, 303 (2022).

[47] R. Nehra, R. Sekine, L. Ledezma, Q. Guo, R. M. Gray, A. Roy, and A. Marandi, Few-cycle vacuum squeezing in nanophotonics, Science **377**, 1333 (2022).

[48] Y. Shaked, Y. Michael, R. Z. Vered, L. Bello, M. Rosenbluh, and A. Pe'er, Lifting the bandwidth limit of optical homodyne measurement with broadband parametric amplification, Nat. Commun. **9**, 609 (2018).

[49] M. Kues, C. Reimer, P. Roztocki, L. R. Cortés, S. Sciara, B. Wetzel, Y. Zhang, A. Cino, S. T. Chu, B. E. Little *et al.*, On-chip generation of high-dimensional entangled quantum states and their coherent control, Nature (London) **546**, 622 (2017).

[50] M. Erhard, M. Krenn, and A. Zeilinger, Advances in high-dimensional quantum entanglement, Nat. Rev. Phys. **2**, 365 (2020).

[51] L. E. Vicent, A. B. U'Ren, R. Rangarajan, C. I. Osorio, J. P. Torres, L. Zhang, and I. A. Walmsley, Design of bright, fiber-coupled and fully factorable photon pair sources, New J. Phys. **12**, 093027 (2010).

Supplementary Materials: Manipulating multiple optical parametric processes in photonic topological insulators

Zhen Jiang[1,2,#], Bo Ji[1,2,#], Yanghe Chen[1,2], Chun Jiang[1,*] and Guangqiang He[1,2†]

[1] *State Key Laboratory of Advanced Optical Communication Systems and Networks, Department of Electronic Engineering, Shanghai Jiao Tong University, Shanghai 200240, China*

[2] *SJTU Pinghu Institute of Intelligent Optoelectronics, Department of Electronic Engineering, Shanghai Jiao Tong University, Shanghai 200240, China*

[#] *These authors contributed equally to this work.*

I. TOPOLOGICAL KAGOME LATTICE

We consider a two-dimensional infinite kagome lattice with C_3 lattice symmetry (lattice constant a), as shown in Fig.S1. We apply the tight-binding model to the lattice, considering only the nearest hopping term in the model. As a result, the Hamiltonian model in momentum space can be given by [1]

$$\hat{H}_0 = \begin{pmatrix} 0 & K + je^{i(\frac{1}{2}k_x + \frac{\sqrt{3}}{2}k_y)a} & K + je^{-i(\frac{1}{2}k_x - \frac{\sqrt{3}}{2}k_y)a} \\ K + je^{-i(\frac{1}{2}k_x + \frac{\sqrt{3}}{2}k_y)a} & 0 & K + je^{-ik_x a} \\ K + je^{i(\frac{1}{2}k_x - \frac{\sqrt{3}}{2}k_y)a} & K + je^{ik_x a} & 0 \end{pmatrix}, \tag{S1}$$

where K and J denote the intra-cell coupling (red dotted line) and inter-cell coupling (blue dotted line), respectively, as depicted in Fig.S1(a). We can write this Hamiltonian in a more general form:

$$\hat{H}_0 = \begin{pmatrix} 0 & a_1 & b_1 \\ a_2 & 0 & c_1 \\ b_2 & c_2 & 0 \end{pmatrix}, \tag{S2}$$

Next, the generalized chiral symmetry operator in kagome lattices can be described as [1]:

$$\Gamma_3 = \begin{pmatrix} 1 & 0 & 0 \\ 0 & e^{i2\pi/3} & 0 \\ 0 & 0 & e^{-i2\pi/3} \end{pmatrix}, \tag{S3}$$

where Γ_3 is the unitary chiral operator with three eigenvalues of 0, $e^{i2\pi/3}$, and $e^{-i2\pi/3}$. For the original Hamiltonian H_0, the Hamiltonians transformed by the unitary chiral operator are given by [2]

$$\hat{H}_1 = \Gamma_3\ H_0\Gamma_3^{-1} = \begin{pmatrix} 0 & e^{-i2\pi/3}a_1 & e^{i2\pi/3}b_1 \\ e^{i2\pi/3}a_2 & 0 & e^{-i2\pi/3}c_1 \\ e^{-i2\pi/3}b_2 & e^{i2\pi/3}c_2 & 0 \end{pmatrix}, \tag{S4}$$

$$\hat{H}_2 = \Gamma_3 H_1\Gamma_3^{-1} = \begin{pmatrix} 0 & e^{i2\pi/3}a_1 & e^{-i2\pi/3}b_1 \\ e^{-i2\pi/3}a_2 & 0 & e^{i2\pi/3}c_1 \\ e^{i2\pi/3}b_2 & e^{-i2\pi/3}c_2 & 0 \end{pmatrix}. \tag{S5}$$

Therefore, these Hamiltonians satisfy $\hat{H}_0 + \hat{H}_1 + \hat{H}_2 = 0$, which reveals that the kagome lattice has generalized chiral symmetry. The generalized chiral symmetry promises that the sum of the respective eigenenergies is zero. The current Hamiltonian is analogous to the Hamiltonian in the Su-Schrieffer-Heager (SSH) model. The introduction of long-range interactions without breaking the chiral symmetry will lead to a change of the topological invariant (bulk polarization).

---

* cjiang@sjtu.edu.cn

† gqhe@sjtu.edu.cn

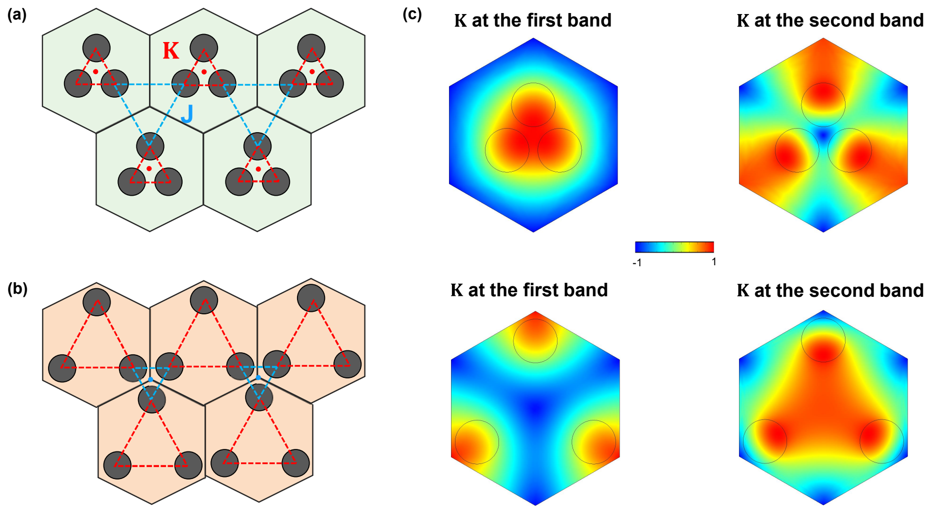

FIG. S1. (a) Shrunken and (b) expanded kagome lattice for trivial and nontrivial cases. (c) Electric field distributions at point K in the first Brillouin zone for two kagome lattices.

To describe the band topology of the kagome lattice with complete symmetry, the bulk polarization is defined as [3]

$$p_s = 1/N_k \sum_{j,k_t} v_s^j(k_t), \tag{S6}$$

where $v_s^j(k_t)$ is the eigenvalue (also denoted as Wannier center) of the Wilson loop. And the eigenvalue problem of the Wilson loops is $W_{k_s+2\pi \leftarrow k_s,k_t}|\nu_k\rangle^j = e^{i2\pi\nu_s^j(k_t)}|\nu_k\rangle^j$, in which $k_s, k_t = 0, \delta k, \ldots, (N_k-1)\delta k, \delta k = \frac{1}{N_k}\frac{4\pi}{\sqrt{3}a}$ and j is the index of the occupied bands. Hence, the Wannier bands associated with the lowest energy band of kagome lattices can be calculated [2]. When the intra-cell coupling K is larger than the inter-cell coupling J (shrunken lattice), the bulk polarization is calculated as 0, which denotes a trivial case (Fig.S1(a)). However, when the intra-cell coupling K is smaller than inter-cell coupling J (expanded lattice), the calculated bulk polarization is 1/3, which denotes a nontrivial case (Fig.S1(b)).

Therefore, according to the bulk–boundary correspondence, the difference in nontrivial polarization gives rise to topological edge states localized at the boundaries between the shrunken and expanded kagome lattices. As shown in Fig.S1(c), the electric field distributions at point K in the first Brillouin zone for two kagome lattices also reveal the topological transition.

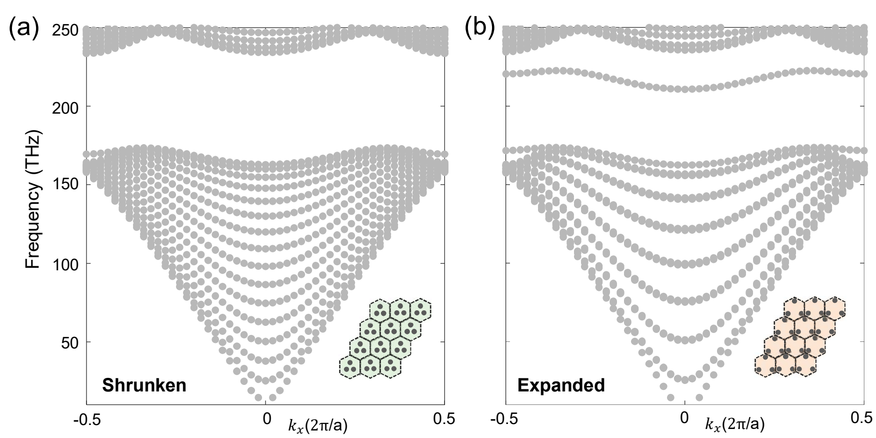

FIG. S2. Calculated dispersion curves for the (a) shrunken ($d = 0.18a$) and (b) expanded ($d = 0.40a$) kagome lattices.

To assess the size of the forbidden frequency gaps for the shrunken ($d = 0.18a$) and expanded ($d = 0.40a$) kagome lattices, we calculate the dispersion curves for the lattice consisting of a single primitive cell. We set the Bloch boundary conditions in all directions and project it in the k_x direction. As illustrated in Fig.S2, the bandgaps of 60 THz (ranging from 173 THz to 233 THz) and 37 THz (ranging from 174 THz to 211 THz) can be observed, indicating the absence of modes within these frequency ranges.

II. THEORETICAL ANALYSIS OF TWO OPPS IN TOPOLOGICAL DEVICES

For the FWM process in our topological device, it contains self-phase modulation (SPM), cross-phase modulation (XPM), and FWM processes. The general nonlinear Hamiltonian can be written by $\hat{H}_{\rm NL} = \hat{H}_{\rm SPM} + \hat{H}_{\rm XPM} + \hat{H}_{\rm FWM}$, we can write all the terms as

$$\begin{aligned}\hat{H}_{\rm NL} = -\hbar\gamma[&\frac{1}{2}(\hat{a}_p^\dagger\hat{a}_p^\dagger\hat{a}_p\hat{a}_p + \hat{a}_s^\dagger\hat{a}_s^\dagger\hat{a}_s\hat{a}_s + \hat{a}_i^\dagger\hat{a}_i^\dagger\hat{a}_i\hat{a}_i)\\ &+ 2(\hat{a}_p^\dagger\hat{a}_s^\dagger\hat{a}_p\hat{a}_s + \hat{a}_p^\dagger\hat{a}_i^\dagger\hat{a}_p\hat{a}_i + \hat{a}_s^\dagger\hat{a}_i^\dagger\hat{a}_s\hat{a}_i)\\ &+ (\hat{a}_s^\dagger\hat{a}_i^\dagger\hat{a}_p\hat{a}_p + \hat{a}_p^\dagger\hat{a}_p^\dagger\hat{a}_s\hat{a}_i)]\end{aligned} \tag{S7}$$

where $\hat{a}_{p,s,i}$ and $\hat{a}^\dagger_{p,s,i}$ and $a^\dagger_{s,\omega_i}$ are the annihilation and creation operators respectively, the effective nonlinearity is $\gamma = \omega_p n_2/cA_{\rm eff}$, and n_2 is the Kerr nonlinearity of silicon with a value of 5×10^{-18} [4], $A_{\rm eff}$ is the nonlinear effective area. The final term (FWM process) is crucial for the energy transfer among the three modes. The SPM and XPM terms significantly influence the oscillation process, as well as the noise and entanglement characteristics of the system. Note that we only consider the FWM process generated in sandwich topological waveguides with a length $L = 400a$. However, the FWM processes in two branches of the diamond-like structure are neglected since the nonlinear interaction length is small.

A. Left branch: OPA process generated from interband OPP

In our setup, we employ optical parametric amplification (OPA) through FWM, combined with interband optical parametric processes (OPP). This approach, utilized within the diamond-like structure, results in the spatial separation of signal photons to the left branch. For the OPA process, we analyze the evolution of quantum states by solving the Heisenberg equation $\frac{d\hat{a}_j}{dt} = \frac{i}{\hbar}[\hat{H}, \hat{a}_j], j \in \{p, s, i\}$. By substituting Eq.S7, we can calculate that the updated Heisenberg equations for the signal and idler modes are

$$\begin{aligned}\frac{d\hat{a}_p}{dt} &= i\gamma[(\hat{a}_p^\dagger\hat{a}_p + 2(\hat{a}_s^\dagger\hat{a}_s + \hat{a}_i^\dagger\hat{a}_i)\hat{a}_p + \hat{a}_s\hat{a}_i\hat{a}_p^\dagger]\\ \frac{d\hat{a}_s}{dt} &= i\gamma[(\hat{a}_s^\dagger\hat{a}_s + 2(\hat{a}_p^\dagger\hat{a}_p + \hat{a}_i^\dagger\hat{a}_i)\hat{a}_s + \hat{a}_i^\dagger\hat{a}_p\hat{a}_p]\\ \frac{d\hat{a}_i}{dt} &= i\gamma[(\hat{a}_i^\dagger\hat{a}_i + 2(\hat{a}_p^\dagger\hat{a}_p + \hat{a}_s^\dagger\hat{a}_s)\hat{a}_i + \hat{a}_s^\dagger\hat{a}_p\hat{a}_p]\end{aligned} \tag{S8}$$

We may explore the interaction of three stationary, co-polarized waves at regular frequencies, characterized by their slowly varying electric fields with complex amplitudes $A_p(x)$, $A_s(x)$, and $A_i(x)$, respectively. The total transverse field $E(x, y, z)$ propagating along the sandwich topological waveguide (x-axis) is given by [5]

$$\begin{aligned}E(x, y, z) =& f(y, z)A(x)\\ =& f(y, z)\frac{1}{2}[A_p(x)\times\exp(ik_0x - i\omega_0t) + A_s(x)\exp(ik_1x - i\omega_1t)\\ &+ A_i(x)\exp(ik_2x - i\omega_2t) + h.c.],\end{aligned} \tag{S9}$$

in which h.c. refers to the complex conjugate. The $f(y, z)$ denotes a common transverse modal profile, which is assumed to be identical for all three waves propagating along the waveguide. According to Eq.S8, we can derive three coupled equations for the classicized field amplitudes of the three waves as [6]

$$\begin{aligned}\frac{dA_p}{dx} &= i\gamma[(|A_p|^2 + 2(|A_s|^2 + |A_i|^2))A_p + 2A_sA_iA_p^*\exp(i\Delta kx)],\\ \frac{dA_s}{dx} &= i\gamma[(|A_s|^2 + 2(|A_i|^2 + |A_p|^2))A_s + A_i^*A_p^2\exp(-i\Delta kx)],\\ \frac{dA_i}{dx} &= i\gamma[(|A_i|^2 + 2(|A_s|^2 + |A_p|^2))A_i + A_s^*A_p^2\exp(-i\Delta kx)],\end{aligned} \tag{S10}$$

Note that the first two terms on the right-hand side of Eq.S10 denote the nonlinear phase shifts due to SPM and XPM, respectively. The last term denotes energy transfer between the interacting waves. By replacing the amplitude of the light field by $A_j(x) = \sqrt{P_j}\exp(i\phi_j)$ for $j \in \{p, s, i\}$, Eq.S10 can be rewritten as [6]

$$\begin{aligned}
\frac{dP_p}{dx} &= -4\gamma\left(P_p^2 P_s P_i\right)^{1/2}\sin\theta,\\
\frac{dP_s}{dx} &= 2\gamma\left(P_p^2 P_s P_i\right)^{1/2}\sin\theta,\\
\frac{dP_i}{dx} &= 2\gamma\left(P_p^2 P_s P_i\right)^{1/2}\sin\theta,
\end{aligned} \tag{S11}$$

and

$$\frac{d\theta}{dx} = \Delta k + \gamma(2P_p - P_s - P_i) + \gamma\left[\left(P_p^2 P_i/P_s\right)^{1/2} + \left(P_p^2 P_i/P_s\right)^{1/2} - 4\left(P_s P_i\right)^{1/2}\right]\cos\theta. \tag{S12}$$

Neglecting the third term in Eq.S12, an approximated result for relative phase difference is given by [5]

$$\frac{d\theta}{dx} \approx \Delta k + \gamma(2P_p - P_s - P_i) \approx \Delta k + 2\gamma P_p. \tag{S13}$$

Eq.S10 describes the amplification of a weak signal propagating along the topological waveguide. To solve the equations, let $\frac{dA_0}{dx} = 0$, then we can get an analytical solution [7]

$$P_s(L) = P_s(0)\left(1 + \left[\frac{\gamma P_p}{g}\sinh(gL)\right]^2\right), \tag{S14}$$

$$P_i(L) = P_s(0)\left[\frac{\gamma P_p}{g}\sinh(gL)\right]^2, \tag{S15}$$

where L is the propagating length of the topological waveguide along x axis. The parametric gain coefficient is given by

$$g^2 = \left[(\gamma P_p)^2 - (\kappa/2)^2\right] = -\Delta k\left[\frac{\Delta k}{4} + \gamma P_p\right]. \tag{S16}$$

Furthermore, the single gain can be given by [5]

$$G_\mathrm{s} = \frac{P_\mathrm{s}(L)}{P_\mathrm{s}(0)} = 1 + \left(\frac{\gamma P_\mathrm{p}}{g}\sinh(gL)\right)^2. \tag{S17}$$

B. Right branch: entangled biphoton state generated from intra-band OPP

After tracing out of interband OPP from the FWM process in our diamond-like structure (left branch), the FWM process propagating along the right branch can be considered as an entangled biphoton state generator. Here we start with the nonlinear Hamiltonian in Eq.S7, by replacing neglecting the weak terms and pump term $\frac{1}{2}(\hat{a}_p^\dagger\hat{a}_p^\dagger\hat{a}_p\hat{a}_p)$, the Hamiltonian of the FWM process can be rewritten by

$$\hat{H}_\mathrm{NL} \approx -\hbar\gamma[2(\hat{a}_p^\dagger\hat{a}_s^\dagger\hat{a}_p\hat{a}_s + \hat{a}_p^\dagger\hat{a}_i^\dagger\hat{a}_p\hat{a}_i) + (\hat{a}_s^\dagger\hat{a}_i^\dagger\hat{a}_p\hat{a}_p + \hat{a}_p^\dagger\hat{a}_p^\dagger\hat{a}_s\hat{a}_i)]. \tag{S18}$$

Here we apply the electric field to replace the operators as

$$\hat{H}_\mathrm{NL} \approx -\hbar\gamma[2(\hat{E}_p^+\hat{E}_p^-\hat{E}_s^+\hat{E}_s^- + \hat{E}_p^+\hat{E}_p^-\hat{E}_i^+\hat{E}_i^-) + (\hat{E}_s^+\hat{E}_i^+\hat{E}_p^-\hat{E}_p^- + \hat{E}_s^-\hat{E}_i^-\hat{E}_p^+\hat{E}_p^+)], \tag{S19}$$

in which the pump field operator is considered as the classical field

$$\hat{E}_p^{(+)}(x,t) = \hat{E}_p^{-*}(x,t) = A_p e^{i(k_p x - \omega_p t)}, \tag{S20}$$

and the quantized field of signal and idler modes are

$$\hat{E}_j^{(-)}(x,t) = \int d\omega_j A_j^* e^{-i(k_j x - \omega_j t)} \hat{a}_j^\dagger(\omega_j), \quad j = s, i, \tag{S21}$$

where the amplitude of the field is $A_j = \sqrt{\frac{\omega_j}{4\pi\varepsilon_0 n_j c A_{\text{eff}}}}$. By substituting Eq.S20 and Eq.S21 into Eq.S19, we can obtain the Hamiltonian as

$$\hat{H}_{\text{NL}} = -\hbar\eta \int_{-\infty}^{\infty} d\omega_s \int_{-\infty}^{\infty} d\omega_i e^{-i(2k_p - k_s - k_i)x} e^{(2\omega_p - \omega_s - \omega_i)t} \hat{a}_s(\omega_s)\hat{a}_i(\omega_i) + h.c., \tag{S22}$$

where the constant term is

$$\eta = \frac{{A_P}^2\gamma}{4\pi\epsilon_0 c A_{\text{eff}}} \sqrt{\frac{\omega_s\omega_i}{n_s n_i}}. \tag{S23}$$

we can calculate the biphoton state generated from the FWM process via first-order perturbation theory by $|\Psi\rangle = \frac{1}{i\hbar}\int_{-\infty}^{\infty} dt H_{NL}|0\rangle$, therefore the biphoton state is given by

$$|\Psi\rangle = \eta \int\int d\omega_s d\omega_i \alpha(\frac{\omega_s + \omega_i}{2}) \operatorname{sinc}(\frac{\Delta kL}{2}) \hat{a}_s^\dagger(\omega_s)\hat{a}_i^\dagger(\omega_i)|0\rangle,. \tag{S24}$$

in which the spectrum $\alpha(\frac{\omega_s+\omega_i}{2}) = 2\pi\delta(\omega_s + \omega_i - 2\omega_p)$, and the joint spectral amplitude (JSA) of biphoton state is [8]

$$\mathcal{A}(\omega_s, \omega_i) = \alpha(\frac{\omega_s + \omega_i}{2}) \operatorname{sinc}(\frac{\Delta kL}{2}). \tag{S25}$$

We use Schmidt decomposition to confirm the entanglement of photon pairs generated via intra-band OPP. The JSA can be decomposed by [8]:

$$\mathcal{A}(\omega_s, \omega_i) = \sum_{n=1}^{N} \sqrt{\lambda_n}\psi_n(\omega_s)\phi_n(\omega_i), \tag{S26}$$

where λ_n ($N \in \mathbb{N}$) represents the Schmidt coefficient, ψ_n and ϕ_n are are orthonormal functions of ω_s and ω_i in the Hilbert space. λ_n, ψ_n and ϕ_n are connected by these equations

$$\begin{aligned} \int K_1(\omega,\omega')\psi_n(\omega')d\omega' &= \lambda_n\psi_n(\omega), \\ \int K_2(\omega,\omega')\phi_n(\omega')d\omega' &= \lambda_n\phi_n(\omega), \end{aligned} \tag{S27}$$

where K_1 and K_2 are the one-photon spectral correlations, and ψ_n and ϕ_n are corresponding eigenfunctions. When the Schmidt number $N > 1$, the biphoton state is considered frequency entangled. The equations can be rewritten as

$$\begin{aligned} K_1(\omega,\omega') &= \int \mathcal{A}(\omega,\omega_i)\mathcal{A}^*(\omega',\omega_i)d\omega_i, \\ K_2(\omega,\omega') &= \int \mathcal{A}(\omega_s,\omega)\mathcal{A}^*(\omega_s,\omega')d\omega_s, \end{aligned} \tag{S28}$$

K_1 and K_2 form $s \times s$ and $i \times i$ matrices respectively. The eigenfunctions can be represented as:

$$\begin{aligned} K_1\psi_n &= \lambda_n\psi_n, \\ K_2\phi_n &= \lambda_n\phi_n, \end{aligned} \tag{S29}$$

Eq.S26 can be rewritten as

$$\mathcal{A} = \sum_{n=1}^{N} \sqrt{\lambda_n}\psi_n\phi_n^T, \tag{S30}$$

Using Eq.S30, the Schmidt coefficients λ_n are determined by solving the eigenvalue equations. Notably, frequency entanglement of biphoton states is confirmed when there is more than one non-zero Schmidt coefficient λ_n, or when the entanglement entropy $S_k > 0$ [8]. Additionally, the entropy of entanglement S_k and Schmidt number K are useful metrics to quantify the degree of entanglement [8]

$$S_k = -\sum_{n=1}^{N} \lambda_n \log_2 \lambda_n, \tag{S31}$$

$$K = -\frac{\left(\sum\limits_{n=1}^{N} \lambda_n\right)^2}{\sum\limits_{n=1}^{N} \lambda_n^2}. \tag{S32}$$

The high values of $K = 16.24$ and $S_k = 4.42$ suggest a high quality of high-dimensional frequency entanglement.

III. IMPLEMENTING MULTIPLE OPPS IN HONEYCOMB LATTICE

A. Topological honeycomb lattice

We then consider conducting multiple OPPs in honeycomb lattices that emulate the QVH effect. We study the valley kink states in topological honeycomb lattices, for undisturbed unit cells with C_6 lattice symmetry, degenerated Dirac points appear in the K and K′ valleys. The effective Hamiltonian near the K (K′) point is expressed as [9–11]

$$H_{K/K'} = \tau_z \nu_D (\sigma_x \delta k_x + \sigma_y \delta k_y). \tag{S33}$$

Here, v_D represents the group velocity, and σ_x and σ_y are the Pauli matrices. $\delta\vec{k} = \vec{k} - \vec{k}_{K/K'}$ indicates the deviation of the wavevector. Introducing unit cell distortion ($d_1 \neq d_2$), the Hamiltonian can be modified as follows

$$H_{K/K'} = \tau_z \nu_D (\sigma_x \delta k_x + \sigma_y \delta k_y) + \tau_z \gamma \sigma_z. \tag{S34}$$

In this expression, $\tau_z = 1(-1)$ denotes the K (K′) valley pseudospin, $\sigma_{x,y,z}$ denotes the Pauli matrices, ν_D is the group velocity, and γ is the strength of the symmetry-breaking perturbation. The perturbations $\gamma 1$ and γ_2 are defined as $\gamma_1 \propto \left[\int_B \varepsilon_z ds - \int_A \varepsilon_z ds\right]$ (VPC1) and $\gamma_2 \propto \left[\int_D \boldsymbol{\varepsilon}_z ds - \int_C \boldsymbol{\varepsilon}_z ds\right]$ (VPC2), respectively, where $\int \varepsilon_z ds$ is the integration of the dielectric constant ε_z at the positions of A and B, respectively. For the given parameters, $d_A = 0.36a$ and $d_B = 0.24a$, resulting in $\int_B \varepsilon_z ds < \int_A \varepsilon_z ds$. Moreover, we find $|\gamma_1| > |\gamma_2|$.

This implies that the modes at the K and K′ valleys exhibit opposite circular polarizations: left-handed circular polarization (LCP) and right-handed circular polarization (RCP), respectively. The valley Chern numbers of VPCs are determined by [10, 11]:

$$C_{K/K'} = \frac{1}{2\pi} \int_{HBZ} \Omega_{K/K'}(\delta\vec{k}) dS = \pm 1/2, \tag{S35}$$

where $\Omega = \nabla_k \times \vec{A}(k)$ is the Berry curvature, and $\vec{A}(k)$ is the Berry connection. This integration region covers half of the Brillouin zone. Thus, the disparity in the valley Chern numbers of the system is calculated as $|C_{K/K'}| = 1$, confirming the topological characteristics of VPCs. These findings indicate that the oscillation patterns at the K and K′ valleys show different polarizations.

B. Multiple OPPs in honeycomb lattices

The silicon-based VPCs are composed of a honeycomb lattice featuring circular holes ($0.13a$ radius) with a lattice constant of $a = 480$ nm. The unperturbed unit cells ($d_1 = d_2$) demonstrate a C_6 symmetry, resulting in the degeneracy of K and K′ valleys in the Brillouin zone. However, breaking the inversion symmetry ($d_1 \neq d_2$) leads to a complete bandgap near the Γ point [9, 10]. Figure S3(a) shows the band diagrams of unperturbed (gray dots) and perturbed (blue dots) honeycomb lattices. There exists a bandgap for perturbed honeycomb lattice due to the breaking of C_6 lattice symmetry.

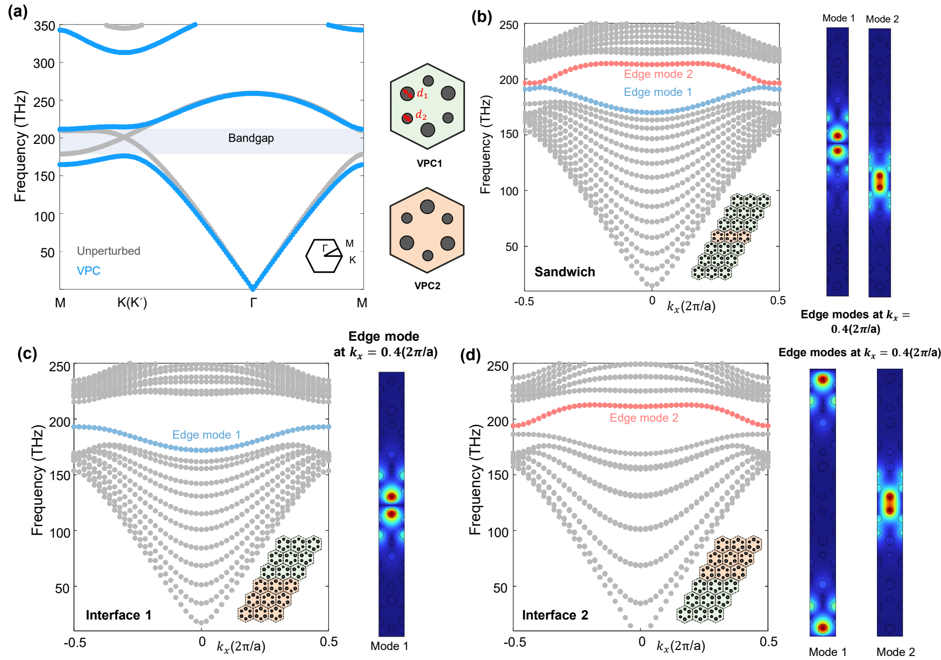

FIG. S3. (a) Band diagrams for unperturbed (gray dots) and perturbed (blue dots) honeycomb lattice. (b) Calculated dispersion curves for the sandwich topological interface. The right insets show the field distributions for two valley kink states with $k_x = 0.4(2\pi/a)$. The structural parameters of VPC1 (VPC2) are $d_1 = 0.36a$ and $d_2 = 0.24a$ ($d_1 = 0.24a$ and $d_2 = 0.36a$). Dispersion relations for the (c) topological interface 1 and (d) topological interface 2, respectively. The right insets show the electric field distributions for different edge modes.

In VPCs, topologically protected edge states, also known as valley kink states [5], are observable at the boundary between VPC1 and VPC2. Similarly, we calculate the band structure of a sandwich topological interface containing both VPC1 and VPC2, as shown in Fig.S3(b). The dispersion curve reveals the existence of two edge modes localized within the topological bandgap. The right insets show the field distributions for two edge modes with $k_x = 0.4(2\pi/a)$, revealing that these two modes are localized in two boundaries. The dispersion relation of the topological interface 1 is depicted in Fig.S3(c), there is one edge mode inside the bandgap. Exchanging the two VPCs leads to the inversion of valley Chern numbers and further facilitates the inversion of topological edge states (Fig.S3(d)). For the topological interface 2, the electric fields of these edge modes are localized differently: one at the outer boundary and the other at the inner boundary.

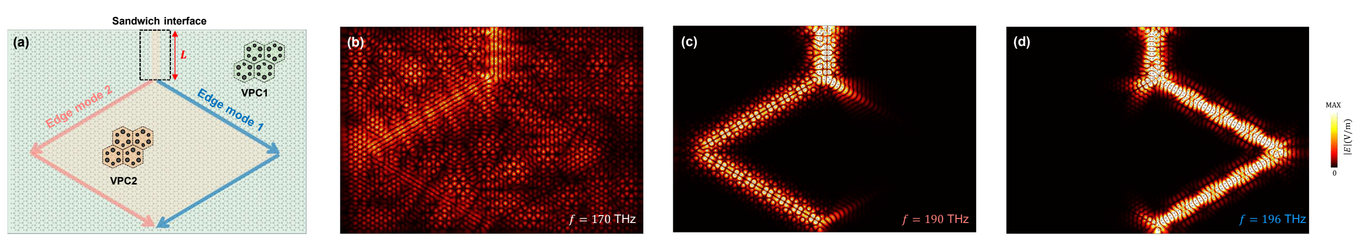

FIG. S4. (a) A design of a topological device composed of VPC1 (green region) and VPC2 (orange region), which contains two parts: a sandwich topological interface (marked by a black dashed box) and a diamond-like topological structure. (b)-(d) Field profiles for edge modes at different frequencies in the topological device.

We also demonstrate a resembling diamond-like structure composed of both VPC1 (green area) and VPC2 (orange area) VPCs, as shown in Fig.S4(a). Due to the mirror symmetry of VPCs, the two edges of the rhombus correspond to topological edge states for topological interfaces 1 and 2, respectively. We simulate the field profiles of field distributions in this diamond-like structure at different frequencies. As shown in Fig.S4(b)-(d), these edge modes can be efficiently transmitted to their respective ports within the different frequency spectrum. This design also results in frequency division functionality, which can be applied to the separation of quantum states.

We simulate the transmission spectra in Fig.S5(a), which demonstrates the frequency division functionality of our diamond-like design. Due to the presence of two edge modes for the sandwich topological interface, the phase-matching intensity distribution of FWM processes depicted in Fig.S5(b) demonstrates two OPPs, including the intra-band OPP and interband OPP between two edge modes, respectively. Correspondingly, the JSA of the biphoton state generated from the FWM process with 190 THz pumping is shown in Fig.S5(c). Likewise, there also exist a main region and two symmetrical bright spots, corresponding to intra-band and interband OPP, respectively. These two OPPs are expected to be performed as entangled biphoton generation and an OPA process (Supplementary Section II). Furthermore, we can obtain the JTA of the biphotons from the Fourier transform of the JSA, as shown in Fig.S5(d), leading to a signal-idler correlation with a bandwidth of 10 ps. More importantly, we have shown that our topological devices that conduct multiple OPPs can be implemented in valley-Hall kagome and honeycomb lattices. Therefore, we believe that multifunctional quantum devices can be fabricated in a broader range of topological structures in the future.

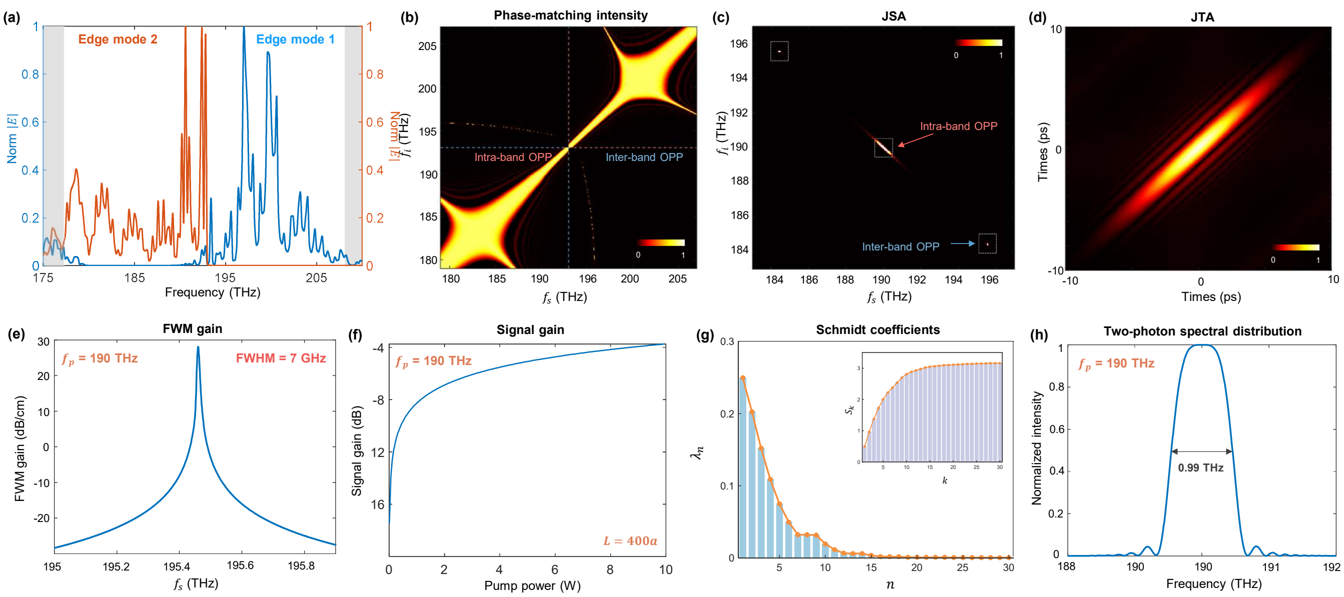

FIG. S5. (a) Normalized electric field monitored by two probes placed at the output ports of the two branches in the diamond-like structure. (b) Phase-matching intensity distribution of FWM processes in the sandwich topological interface. (c) JSA distribution and (d) corresponding JTA distribution characterizing the biphoton state generated in the sandwich topological interface. (e) FWM gain coefficient corresponding to the interband OPP at the 190 THz pump frequency for a $400a$ length topological waveguide. (f) Signal gain as a function of pump power. (g) Normalized Schmidt coefficients λ_n and entanglement entropy S_k for the biphoton state generated from intra-band OPP. (h) Normalized two-photon spectral distribution at the 190 THz pump frequency.

C. OPA and entangled biphoton generation from different OPPs

In this section, we show that our topological honeycomb lattice can be used to implement two functionalities: OPA and the generation of entangled photon pairs. First, we consider the OPA through FWM with interband OPP. The frequency division in the diamond-like structure results in the spatial separation of signal photons, facilitating the straightforward extraction of amplified optical signals. Figure S5(e) shows the FWM gain coefficient corresponding to the intra-band OPP at the 190 THz pump frequency for a $400a$ length topological sandwich waveguide (1 W pump power). Interband OPP excites a super-narrow bandwidth of significant amplification, with a full width at half maximum (FWHM) of about 7 GHz. At the center frequency of the gain range, an FWM gain coefficient of up to 30 dB/cm can be achieved. Such a tunable narrow-bandwidth OPA is particularly useful for amplifying signals from a single-photon source. Fig. S5(f) shows the signal gain as a function of pump power.

In addition, we conduct the generation and control of a frequency-entangled biphoton state originating from the intra-band OPP. In particular, the pump, signal, and idler modes can all be coupled into the left branch of the diamond-like topological structure. This setup is advantageous for directly extracting broadband entangled photon pairs from this boundary. We apply Schmidt decomposition to evaluate the separability of the JSA [8]. Figure S5(g) displays the distributions of normalized Schmidt coefficients λ_n and entanglement entropy S_k, respectively. For our

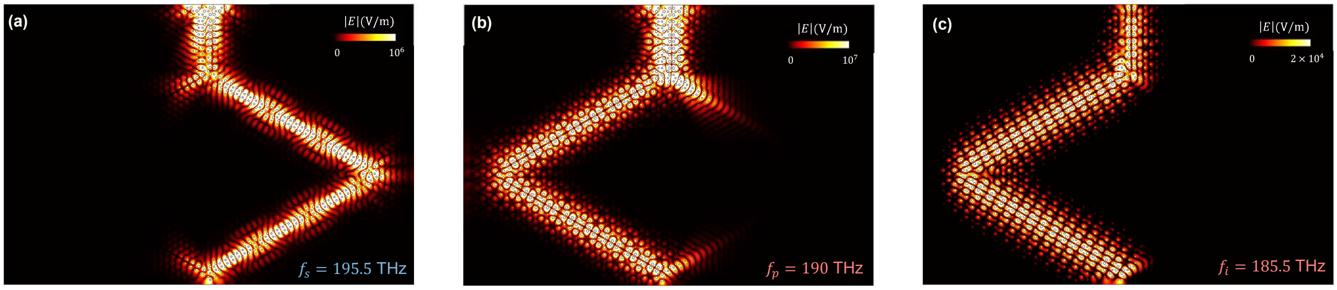

FIG. S6. Field profiles of the FWM process in the diamond-like VPC structure at the frequencies of the (a) signal mode ($f_s = 195.5$ THz), (b) pump mode ($f_p = 190$ THz), and (c) idler mode($f_i = 184.5$ THz), respectively.

topological quantum state, the calculated values for the Schmidt number and entanglement entropy are $K = 6.67$ and $S_k = 3.16$, respectively, demonstrating the presence of a high-quality frequency-entangled biphoton state in the sandwich topological interface. We then calculate the normalized two-photon spectral distribution at the pump frequency of 190 THz. Figure S5(h) illustrates that the 3 dB bandwidth of the two-photon spectrum is 0.99 THz. These properties demonstrate a key feature of our high-dimensional topological quantum entangled state.

Furthermore, we perform simulations of the FWM in a diamond-like topological structure with CW pump excitation. The frequencies for the pump, signal, and idler modes are set at $f_s = 195.5$ THz, $f_p = 190$ THz, and $f_i = 184.5$ THz, respectively. As illustrated in Fig.S6(a)-(c), the field profiles at the idler frequency demonstrate the FWM process within the topological edge modes. In particular, due to their different frequencies, the signal mode is coupled to the left side of the diamond-like structure, while the pump and generated idler mode are directed to the right branch.

[1] X. Ni, M. Weiner, A. Alu, and A. B. Khanikaev, Observation of higher-order topological acoustic states protected by generalized chiral symmetry, Nature Materials **18**, 113 (2019).

[2] M. Li, D. Zhirihin, M. Gorlach, X. Ni, D. Filonov, A. Slobozhanyuk, A. Alù, and A. B. Khanikaev, Higher-order topological states in photonic kagome crystals with long-range interactions, Nature Photonics **14**, 89 (2020).

[3] R. King-Smith and D. Vanderbilt, Theory of polarization of crystalline solids, Physical Review B **47**, 1651 (1993).

[4] A. L. Gaeta, M. Lipson, and T. J. Kippenberg, Photonic-chip-based frequency combs, Nature Photonics **13**, 158 (2019).

[5] J. Hansryd, P. A. Andrekson, M. Westlund, J. Li, and P.-O. Hedekvist, Fiber-based optical parametric amplifiers and their applications, IEEE Journal of Selected Topics in Quantum Electronics **8**, 506 (2002).

[6] G. Cappellini and S. Trillo, Third-order three-wave mixing in single-mode fibers: exact solutions and spatial instability effects, JOSA B **8**, 824 (1991).

[7] R. Stolen and J. Bjorkholm, Parametric amplification and frequency conversion in optical fibers, IEEE Journal of Quantum Electronics **18**, 1062 (1982).

[8] C. Law, I. A. Walmsley, and J. Eberly, Continuous frequency entanglement: effective finite hilbert space and entropy control, Physical Review Letters **84**, 5304 (2000).

[9] Y. Yang, Y. Yamagami, X. Yu, P. Pitchappa, J. Webber, B. Zhang, M. Fujita, T. Nagatsuma, and R. Singh, Terahertz topological photonics for on-chip communication, Nature Photonics **14**, 446 (2020).

[10] J. Lu, C. Qiu, L. Ye, X. Fan, M. Ke, F. Zhang, and Z. Liu, Observation of topological valley transport of sound in sonic crystals, Nature Physics **13**, 369 (2017).

[11] J. Noh, S. Huang, K. P. Chen, and M. C. Rechtsman, Observation of photonic topological valley hall edge states, Physical Review Letters **120**, 063902 (2018).